Chapter 1
Damage Identification for Beam-Like Structures Based on Physics-Informed Neural Networks

Wei Zhou and Y. F. Xu

Abstract Damage in a beam-like structure due to decreases in its stiffness and/or mass can cause local anomalies in its flexural guided wavefield at locations of damage. Usually, these local anomalies can be intensified by data-driven techniques such as the continuous wavelet transform, the gapped smoothing method, etc. However, the physics of beam-like structures are not considered in these data-driven techniques, leading to a lack of physical consistency in the damage identification results. In this paper, a baseline-free damage identification method is proposed to extract these local anomalies under the assumption that the pristine beam-like structures are homogeneous and isotropic. Flexural guided wavefield of a damaged beam-like structure is used to build a pseudo-pristine model of the beam-like structure by using physics-informed neural networks. When the pseudo-pristine model is built, the prediction of flexural guided wavefield can be generated, and those local anomalies can be approximated by the difference between the prediction of flexural guided wavefield and the corresponding measured flexural guided wavefield. The difference is used to yield an accumulative two-dimensional damage index for further damage identification. Effectiveness and noise-robustness of the proposed method are investigated in a numerical example. Results show that the proposed method is effective and noise-robust in identifying the location and extent of the damage.

Keywords Structural damage identification · Physics-informed neural networks · Pseudo-pristine model · Beam-like structures · Local anomalies

1.1 Introduction

Engineering structures in service suffer from long-term environmental effects and operational loads, which cause unexpected structural damage. Monitoring structural damage is important for preserving and sustaining the service life of engineering structures. It is necessary to monitor structural damage by developing noise-robust and accurate damage identification methods. Recently, machine learning and especially deep learning algorithms have been studied widely in damage identification methods, thanks to the rapid development of graphics processing units (GPUs) and sensing technology in the last decade, including acoustic emission-based methods [1], guided wavefield-based methods [2], vibration-based structural damage identification methods [3, 4], etc.

Guided wavefield-based methods have been studied widely for damage Identification, owing to the capability of scanning laser Doppler vibrometers (SLDVs), which can measure velocities of a structure on each point of a predefined grid. It allows the visualization and post-processing of a guided wavefield by reconstructing measured velocities [5]. Joseph et al. [6] proposed a guided wavefield-based method for damage detection in thin metal plates. It uses full wavefield data acquired by SLDV, half from the damaged state and another half from the undamaged state, to train a deep neural network with two convolutional layers and two fully connected layers. It was reported that their proposed method has a better performance than support vector machine-based methods. Abdalraheem et al. [2] proposed guided wavefield-based method for damage detection by using deep fully convolutional neural networks (CNNs) FCN-DenseNet. It was fed by a large dataset of guided wavefields, which contains 475 cases of guided wavefields resulting from interaction with delaminations of random shape, size, and location. The results reveal that their proposed method performs better than the adaptive wavenumber filtering method. Besides, the same dataset has been used in a comparative study for delamination identification by using several deep

W. Zhou · Y. F. Xu (✉)
Department of Mechanical and Materials Engineering, University of Cincinnati, Cincinnati, OH, USA
e-mail: zhouw6@mail.uc.edu; xu2yf@uc.edu

M. Allen et al. (eds.), *Special Topics in Structural Dynamics & Experimental Techniques, Volume 5*,
Conference Proceedings of the Society for Experimental Mechanics Series, https://doi.org/10.1007/978-3-031-37007-6_1

fully CNNs models, including VGG16 encoder-decoder, PSPNet, residual UNet, and FCN-DenseNet [7]. It was reported that GCN model has the highest identification accuracy among the five implemented models. Song et al. [8] proposed guided wavefield-based method for identifying sub-wavelength defects. It combines two distinct fully CNNs, including a global detection network and a local super-resolution network. It was reported that their proposed method can not only locate sub-wavelength defects but also estimate the shape and size of the identified sub-wavelength defects. The aforementioned methods require labeled dataset which not only contains guided wavefields but also contains corresponding information of damage. However, labels are usually unavailable in practice, or acquiring these datasets are very time-consuming. Hence, it is necessary for researchers to come up with innovative methods using guided wavefields without labels under machine learning or deep learning applications.

Physics-informed neural networks (PINNs) are a mesh-free scientific machine learning technique used to solve equations, like nonlinear partial differential equations [9]. PINNs approximate solutions of equations by training a multilayer perceptron neural network to minimize a loss function, which includes terms reflecting the equations residual at selected points in the spatial-temporal domain, and the initial as well as boundary conditions along boundaries of the domain [10]. PINNs have been applied in several works with the ability of incorporating data and their governing physics equation, especially solving inverse problems, where unknown parameters of equation are estimated. Shukla et al. [11] used a PINN to identify a surface breaking crack in a metal plate. Measured ultrasonic surface acoustic waves of the metal were target of the PINN, and a wave velocity field of the metal plate was estimated as a damage index. Rathod et al. [12] identified the change of a wave velocity in a rod by a trained PINN, where 50% reduction in Young's modulus in the mid part can be represented in the identified wave velocity along the rod, but the sharp variation in the wave velocity was not captured. Zhang et al. [13] presented a general framework based on PINNs for solving inverse problems involving unknown material properties and geometric in continuum solid mechanics. It was reported that the framework can accurately estimate the unknown material properties and geometric with a relative error in the order of 10^{-2}.

In this paper, a guided wavefields-based damage identification method based on PINNs is proposed for beam-like structures. In this proposed method, a pseudo-pristine beam model is constructed by a PINN from a measured flexural guided wavefield of a damaged beam-like structure. The residual of Euler–Bernoulli equation with an unknown parameter α, i.e., the ratio of bending stiffness and mass per unit length, is used in the PINN as a loss term. This parameter serves as a variable and is updated in each iteration of gradient descent during the training process of the pseudo-pristine beam model. A predicted flexural guided wavefield is obtained from the pseudo-pristine beam model when the PINN is trained. An accumulative two-dimensional damage index is calculated based on the difference between the measured flexural guided wavefield and the predicted flexural guided wavefield. The location and extent of damage can be identified by consistently high values of the damage index. Accuracy and noise-robustness of the proposed method are investigated in a numerical example of a damaged beam-like structure with different noise levels.

The rest of the paper is arranged as follows. In Sect. 1.2, the proposed damage identification method based on PINNs is presented. In Sect. 1.3, the numerical investigation is described. Conclusions of this work are presented in Sect. 1.4.

1.2 Methodology

1.2.1 Euler–Bernoulli Beam

Consider a narrow, long beam with a lateral load applied, and, consequently, its displacement is off the centerline. The type of dynamic behavior is called flexural motion [14]. In this study, the Euler–Bernoulli beam model is considered. It is a simplification of the linear theory of elasticity which governs the flexural motion of beams. Assuming a pristine beam-like structure is homogeneous undamped, hence its governing equation of flexural motion on a bounded spatial-temporal domain is defined by [15]

$$EI\frac{\partial^4 u\left(x,t\right)}{\partial x^4}+\mu\frac{\partial^2 u\left(x,t\right)}{\partial t^2}=p\left(x,t\right),\quad x\in[0,L],\ \text{and}\ t\in[0,T] \tag{1.1}$$

where $u\left(x,t\right)$ is the spatial-temporal flexural motion of the beam with L spatial lengths and T temporal lengths, E is the elastic modulus, I is the second moment of area of the beam's cross sections, μ is the mass per unit length of the beam, and

$p(x,t)$ is the external force. Divide by μ in each term of Eq. (1.1), and one has

$$\alpha \frac{\partial^4 u(x,t)}{\partial x^4} + \frac{\partial^2 u(x,t)}{\partial t^2} = \frac{p(x,t)}{\mu} \tag{1.2}$$

where

$$\alpha := \frac{EI}{\mu} \tag{1.3}$$

It is observed that Eqs. (1.1) and (1.2) are fourth-order partial differential equations in space, and second order in time.

1.2.2 PINNs for the Euler–Bernoulli Beam

Let $\mathcal{N}(\mathbf{s};\boldsymbol{\theta})$: $\mathbb{R}^{d_s} \rightarrow \mathbb{R}^{d_y}$ be a multilayer perceptron neural network with input vector $\mathbf{s}$, H hidden layers, an output vector $\mathbf{y}$, and trainable network parameters $\boldsymbol{\theta}$. In the h-th hidden layer, N_h number of neurons is present. Each hidden layer receives an input $\mathbf{s}^{h-1} \in \mathbb{R}^{N_{h-1}}$ from the output of the previous layer through the following nested transformations:

$$\mathcal{Q}_h := \sigma^h \left(\mathbf{w}^h \mathbf{s}^{h-1} + \mathbf{b}^h\right), \quad h = 1, \ldots, H \tag{1.4}$$

where σ^h is the nonlinear activation function in the h-th hidden layer, $\mathbf{w}^h \in \mathbb{R}^{N_h \times N_{h-1}}$ and $\mathbf{b}^h \in \mathbb{R}^{N_h}$ are weight matrices and bias vectors in the h-th hidden layer, respectively. Output layer has the similar transformations in Eq. (1.4) but without nonlinear activation. Hence, the final neural network representation can be expressed as

$$\mathcal{N}(\mathbf{s};\boldsymbol{\theta}) = \mathbf{w}^{H+1}\left(\mathcal{Q}_H \circ \mathcal{Q}_{H-1} \circ \cdots \circ \mathcal{Q}_1\right) + \mathbf{b}^{H+1} \tag{1.5}$$

where the operator $\circ$ is the composition operator, $\mathbf{w}^{H+1} \in \mathbb{R}^{N_H}$ and $\mathbf{b}^{H+1} \in \mathbb{R}$ are weight and bias parameters of the output layer, respectively. Hence, all trainable network parameters can be represented as $\boldsymbol{\theta} = \left\{\mathbf{w}^1, \mathbf{b}^1, ..., \mathbf{w}^{H+1}, \mathbf{b}^{H+1}\right\}$. With reference to the universal approximation theorem [16], $u(\mathbf{x},\mathbf{t})$ can be approximated by

$$u(\mathbf{x},\mathbf{t}) \approx \mathcal{N}(\mathbf{x},\mathbf{t};\boldsymbol{\theta}) \tag{1.6}$$

where $\mathbf{x} = \{x : x \in [0, L]\}$ and $\mathbf{t} = \{t : t \in [0, T]\}$ are input vectors of $\mathcal{N}(\mathbf{x},\mathbf{t};\boldsymbol{\theta})$. Based on the governing equation of the beam, i.e., Eq. (1.2), the partial differential equation residual $\mathcal{R}(\mathbf{x},\mathbf{t})$ is defined as

$$\mathcal{R}(\mathbf{x},\mathbf{t}) := \alpha \frac{\partial^4 \mathcal{N}(\mathbf{x},\mathbf{t};\boldsymbol{\theta})}{\partial \mathbf{x}^4} + \frac{\partial^2 \mathcal{N}(\mathbf{x},\mathbf{t};\boldsymbol{\theta})}{\partial \mathbf{t}^2} - \frac{p(\mathbf{x},\mathbf{t})}{\mu} \tag{1.7}$$

The value of α is unknown, which updates in each iteration of gradient descent in the training process. Note that $\boldsymbol{\theta}$ can be learned by minimizing the following composite loss function:

$$\mathcal{L}(\boldsymbol{\theta}) = \lambda \mathcal{L}_d(\boldsymbol{\theta}) + \mathcal{L}_r(\boldsymbol{\theta}) \tag{1.8}$$

where

$$\mathcal{L}_d(\boldsymbol{\theta}) = \frac{1}{N_d} \sum \left(\hat{u}(\mathbf{x}_d,\mathbf{t}_d) - \mathcal{N}(\mathbf{x}_d,\mathbf{t}_d;\boldsymbol{\theta})\right)^2 \tag{1.9}$$

$$\mathcal{L}_r(\boldsymbol{\theta}) = \frac{1}{N_d} \sum \left(\mathcal{R}(\mathbf{x}_d,\mathbf{t}_d)\right)^2 \tag{1.10}$$

are residual loss and data loss, respectively. Here, λ is a hyperparameter that is larger than 0, and N_d denotes the number of inputs $\{\mathbf{x}_d, \mathbf{t}_d\}$ in each channel, which can be randomly sampled from the spatial-temporal domain $[0, L] \times [0, T]$, and

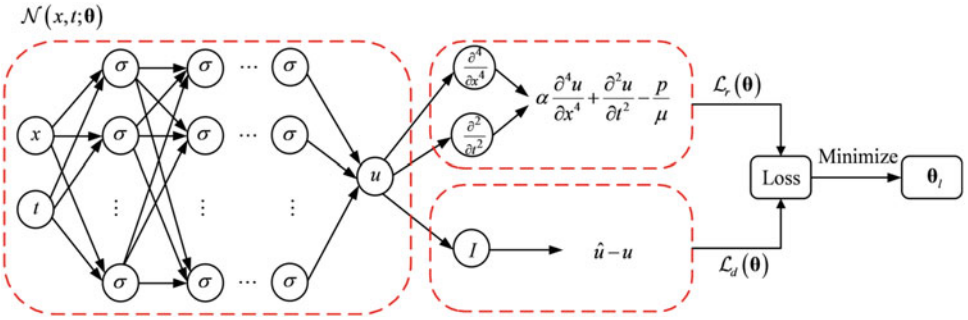

Fig. 1.1 Block diagram of the PINN model for the Euler–Bernoulli beam

$\hat{u}(\mathbf{x}_d, \mathbf{t}_d)$ is a sampled dataset from the measured flexural guided wavefield with corresponding coordinates $\{\mathbf{x}_d, \mathbf{t}_d\}$. The finally learned trainable network parameters are defined as $\boldsymbol{\theta}_l$. A block diagram describing the PINN model used in this study is shown in Fig. 1.1.

1.2.3 Damage Identification Process

Damage in a homogeneous beam-like structure can cause structural flexural motion anomalies at locations of damage although such local anomalies may not be apparent from the measured flexural motion [17]. In the piecewise form, $\hat{u}(x,t)$ can be written as a sum of three components, including the flexural motion for corresponding the pristine structure $\hat{u}_t(x,t)$, local anomalies $\hat{u}_p(x,t)$, if existing, and white noise $\hat{u}_n(x,t)$, if existing, and $\hat{u}(x,t)$ can be expressed by

$$\hat{u}(x,t) = \hat{u}_t(x,t) + \hat{u}_p(x,t) + \hat{u}_n(x,t) \tag{1.11}$$

When a surrogate model learned from $\hat{u}(x,t)$ by PINNs, $\mathcal{N}(x,t;\boldsymbol{\theta}_l)$ is close to $\hat{u}_t(x,t)$. Hence, the difference between $\hat{u}(x,t)$ and $\mathcal{N}(x,t;\boldsymbol{\theta}_l)$ can eliminate most effect from $\hat{u}_t(x,t)$:

$$\triangle u(x,t) = \hat{u}(x,t) - \mathcal{N}(x,t;\boldsymbol{\theta}_l) \tag{1.12}$$

When $\hat{u}(x,t)$ is measured from a pristine beam, $\triangle u(x,t)$ will contain errors of the surrogate model and $\hat{u}_n(x,t)$. On the other side, $\triangle u(x,t)$ will contain one more term, i.e., $\hat{u}_p(x,t)$, than the former one, when $\hat{u}(x,t)$ is measured from a damaged beam. Hence, unapparent local anomalies in $\hat{u}(x,t)$ will become dominated in $\triangle u(x,t)$ when damage exists.

An accumulative two-dimensional damage index can be constructed for damage identification for accumulating local anomalies, and alleviating the adverse effect of noise and errors in $\triangle u(x,t)$, which is defined as

$$\delta(x,m) = \left(\frac{\sum_{t=0}^{T} |\triangle u(x,t)|}{\max\left(\sum_{t=0}^{T} |\triangle u(x,t)|\right)} \right)^m, \quad m \in [1,\infty) \tag{1.13}$$

where $|\cdot|$ denotes the absolute value of a function and $\max(\cdot)$ is the maximum of a function. With increasing the value of m, the small values of $\delta(x,m)$ responding to noise and errors can be eliminated ultimately. While too large value of m can also lower the value of $\delta(x,m)$ in locations of damage. In this study, m is chosen in [1, 10] for all cases of $\delta(x,m)$. Note that $\delta(x,m) \in [0,1]$ and damage can be identified in neighborhoods with consistently high values of $\delta(x,m)$ with different values of m. A flowchart summarizing the proposed damage identification method is shown in Fig. 1.2.

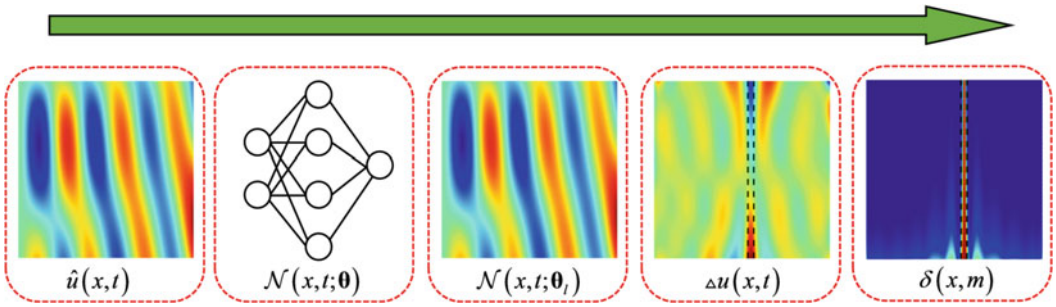

Fig. 1.2 Flowchart of the proposed damage identification method

1.3 Numerical Investigation

In this section, flexural guided wavefields obtained from numerical simulations of two cantilever beams: one is a pristine beam and the other is a damage beam which is generated from the pristine beam with damage in form of a thickness reduction area. The former one is used to study the capability of modeling by PINNs in constructing a surrogate model for the pristine beam. The latter one is used to study the effectiveness of the proposed damage identification method. Besides, the noise-robustness of the method is also investigated and discussed.

1.3.1 Numerical Models of Two Cantilever Beams

For the pristine cantilever beam, it has a height of 6 mm, a width of 3 mm, and a length of 300 mm. The damaged cantilever beam has the same dimensions as the pristine beam, and damage is introduced by a one-sided through-width thickness reduction area with a length of 10 mm and a depth of 0.3 mm. Dimensions of these two beams and the location of the damage are shown in Fig. 1.3. The pristine beam and damaged beam are made of aluminum 6061-T6 with a mass density of 2700 kg/m^3, Young's modulus of 68.9 GPa, and Poisson's ratio of 0.33. The ratio of bending stiffness and mass per unit length, i.e., α, is 19.1389 $\left(\mathrm{m}^4/\mathrm{s}^2\right)$ for the pristine beam. Their numerical model is modeled by the finite element method in finite element analysis software ABAQUS. The models of these two beams are built with the linear eight-node brick (C3D8R) elements. The size of elements is 0.3 mm so that a total of 1001 nodes are evenly distributed along the length of the intact side of each beam. These two cantilever beams are under zero initial conditions, and their free ends are subjected to a five-count wave packet force, which is expressed by

$$h(t) = A\left(H(t) - H\left(t - \frac{5}{f_c}\right)\right)\left(1 - \cos\left(\frac{2\pi f_c t}{5}\right)\right)\sin(2\pi f_c t) \tag{1.14}$$

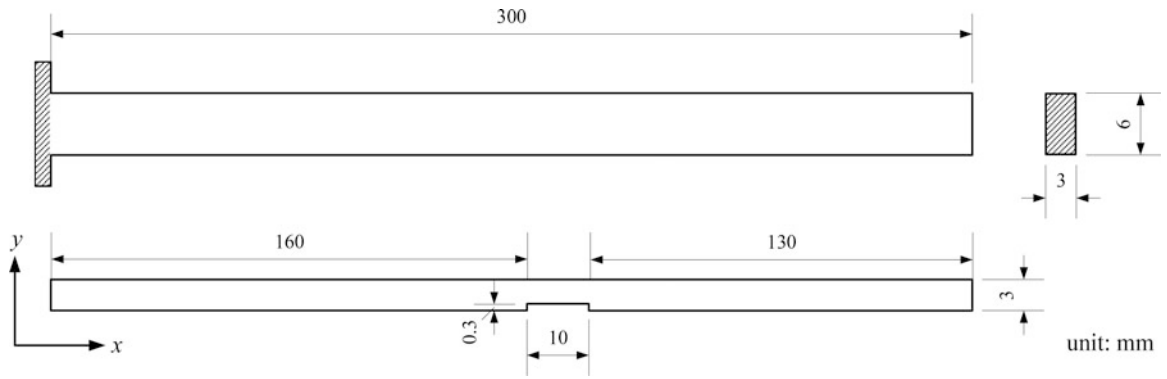

Fig. 1.3 Dimensions of the pristine beam and damaged beam, and the location of the damage on the damaged beam

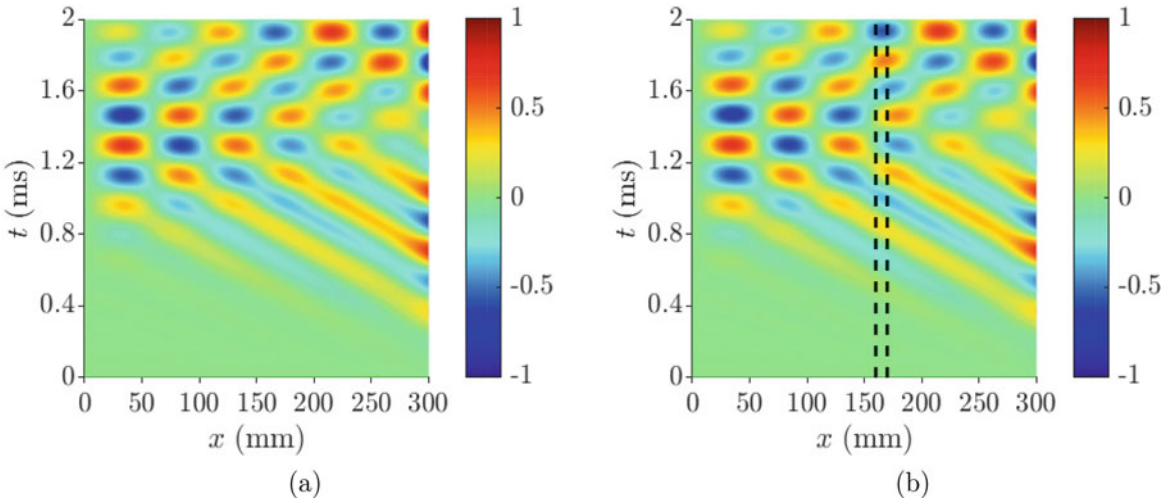

Fig. 1.4 Flexural guided wavefields for (**a**) the pristine beam and (**b**) the damaged beam. The amplitudes of the flexural guided wavefield shown in each figure are normalized for better comparison. Edges of the damage area are depicted by vertical dotted lines

where A defines the magnitude of the force, H is Heaviside function expressed by

$$H(t) = \begin{cases} 1, & t \geqslant 0 \\ 0, & t < 0 \end{cases} \tag{1.15}$$

and f_c is the central frequency of the force. The values of A and f_c are chosen to be 0.5 N and 3 kHz, respectively. The force is only applied in the free end nodes of two beams, and other nodes of beams are zeros. Hence, the force field, i.e., the rightmost item, is approximated by zeros in $\mathcal{R}(\mathbf{x}, \mathbf{t})$ of Eq. (1.7).

Two flexural guided wavefields for the pristine beam and damaged beam are obtained on a grid with 1001 nodes that are evenly distributed along the length of the intact side of each beam and 2501 steps in 2 ms after the excitation force is applied. These flexural guided wavefields are shown in Fig. 1.4. Figure 1.4a shows the flexural guided wavefield consists of a wave packet that is generated from the excitation point and propagating toward the fixed end, and reflecting back to the free end. In Fig. 1.4b, similar observations can be made regarding the resulted flexural guided wavefield for the damaged beam. Besides, reflections and/or local anomalies cannot be directly observed near the damage area.

1.3.2 Numerical Verification Process

The capability of modeling by PINNs is first investigated based on the flexural guided wavefield obtained from the pristine beam. PINNs are notoriously hard to train especially when high-frequency or multi-scale behavior exists [18]. In this study, the spatial-domain frequency is lowered by scaling $\mathbf{x} = \{x : x \in [0, 0.3]\}$ with unit of meter to $\bar{\mathbf{x}} = \{\bar{x} : \bar{x} \in [0, 1]\}$. In the temporal domain, only part of ranges are used and then scale $\mathbf{t} = \{t : t \in [t_1, t_2]\}$ with unit of second to $\bar{\mathbf{t}} = \left\{\bar{t} : \bar{t} \in [t_1/t_2, 1]\right\}$. Besides, the amplitudes of corresponding flexural motion are scaled to the interval $[-1, 1] \in \mathbb{R}$ as follows

$$\bar{u}(x, t) = -1 + 2 \times \frac{\hat{u}(x, t) - \min\left(\hat{u}(x, t)\right)}{\max\left(\hat{u}(x, t)\right) - \min\left(\hat{u}(x, t)\right)}, \quad t \in [t_1, t_2] \tag{1.16}$$

where $\min(\cdot)$ is the minimum of a function. Two models, i.e., model #1 and #2, are built based on two different ranges of the temporal domain to verify the consistence of modeling by PINNs, and they are $t \in [0.5, 0.7] \times 10^{-3}$ s and $t \in [1, 1.2] \times 10^{-3}$ s, respectively. A three-layer fully connected neural network with 100 neurons per hidden layer is used in each model. Two input channels exist in the neural network and number of $N_d = 20{,}000$ points $\left\{\bar{x}_i, \bar{t}_i\right\}_{i=1}^{N_d}$ which are randomly sampled from the selected spatial-temporal domain. The corresponding $\left\{\bar{u}\left(\bar{x}_i, \bar{t}_i\right)\right\}_{i=1}^{N_d}$ are sampled from the scaled flexural guided

wavefield $\bar{u}\left(\bar{\mathbf{x}}, \bar{\mathbf{t}}\right)$. The target function is used as the nonlinear activation function in the two models. The hyperparameter λ in the loss function Eq. (1.8) is set to 10^5. A two-phase optimizer is used to minimize the loss function. In the first phase, the Adam optimizer [19] with a learning rate of 10^{-3} and a weight decay of 10^{-5} is used via 50,000 iterations of gradient descent. In the second phase, the L-BFGS optimizer [20] with a learning rate of 10^{-1} is used until the two models are converged.

The capability of the proposed damage identification method is investigated based on the flexural guided wavefield from the damaged beam. Two pseudo-pristine beam models, i.e., model #3 and #4, are trained under the same setups as the model #1 and #2 with different $\left\{\bar{u}\left(\bar{x}_i, \bar{t}_i\right)\right\}_{i=1}^{N_d}$ sampled from the damaged beam, respectively. When the model #3 and #4 are trained, a damage index is calculated based on Eq. (1.13) for damage identification. Besides, the noise robustness of the proposed damage identification method is investigated. Model #5 is trained under the same setups as the model #4 with noise-contaminated $\left\{\bar{u}\left(\bar{x}_i, \bar{t}_i\right)\right\}_{i=1}^{N_d}$, which is sampled from noise-contaminated flexural guided wavefield. It is generated by adding a Gaussian noise with a signal-to-noise ratio of 30 dB to the flexural guided wavefield obtained from the damaged beam.

1.3.3 Numerical Verification Results

The model #1 is trained after 50,200 iterations of gradient descent, and its results are shown in Fig. 1.5. It can be seen that $\mathcal{L}_r$ is smaller than $\mathcal{L}_d$ at the initial iterations, but $\mathcal{L}_r$ increases radially under the effect of λ and then generally decreases

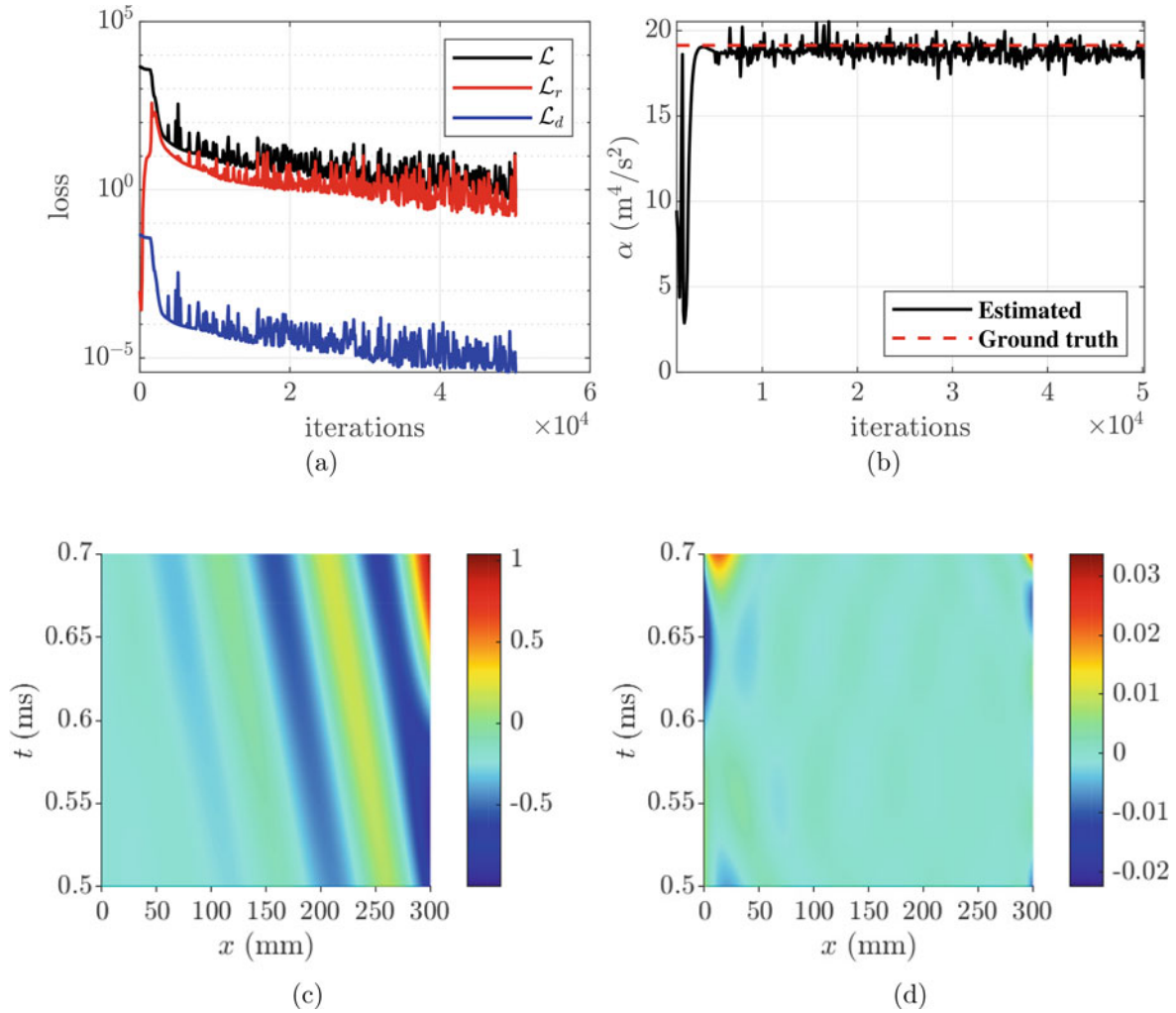

Fig. 1.5 Results for the model #1: (**a**) the composite loss $\mathcal{L}$, the residual loss $\mathcal{L}_r$, and the data loss $\mathcal{L}_d$ with iterations; (**b**) comparison of the estimated value of α and the ground truth of α; (**c**) the prediction of flexural guided wavefield; and (**d**) the difference between the predicted wavefield and the corresponding measured wavefield

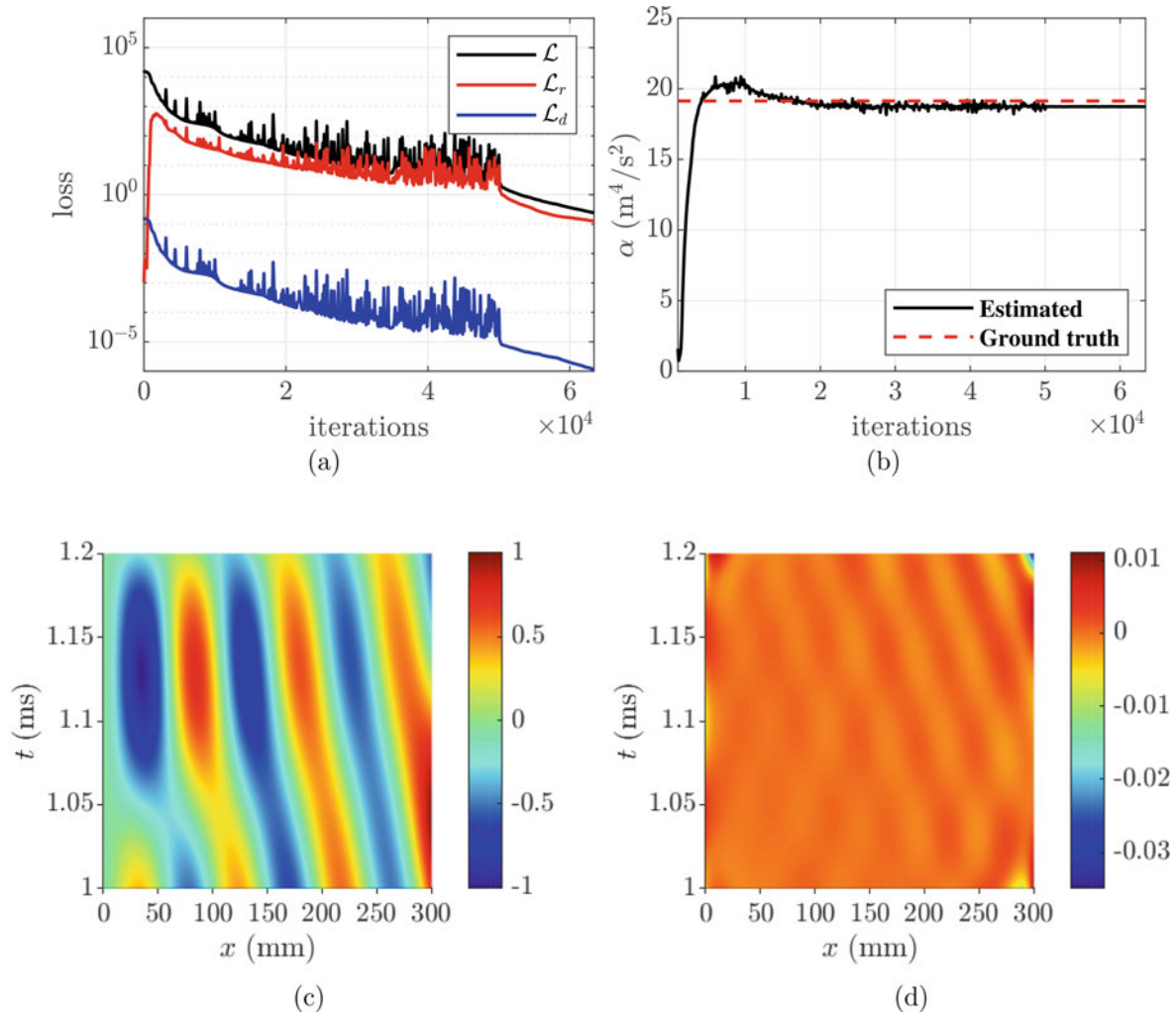

Fig. 1.6 Results for the model #2: (**a**) the composite loss $\mathcal{L}$, the residual loss $\mathcal{L}_r$, and the data loss $\mathcal{L}_d$ with iterations; (**b**) comparison of the estimated value of α and the ground truth of α; (**c**) the prediction of flexural guided wavefield; and (**d**) the difference between the predicted wavefield and the corresponding measured wavefield

as same to $\mathcal{L}_d$ as shown in Fig. 1.5a. The estimated α needs to be divided by a factor of $\left(L^4/t_2^2\right)$ with $L = 0.3$ m and $t_2 = 0.7 \times 10^{-3}$ s due to the scaling in spatial and temporal coordinates in the model #1. The estimated α with iterations is shown in Fig. 1.5b. It can be seen that the estimated α is always nearby the ground truth after approximately 0.5×10^4 iterations. The final estimated α is 18.7446 $\left(\mathrm{m}^4/\mathrm{s}^2\right)$, and the relative error to the ground truth is 2.06%. The prediction of flexural guided wavefield by the model #1 is shown in Fig. 1.5c, and the difference between the predicted wavefield and the corresponding measured wavefield is shown in Fig. 1.5d. Small magnitudes are dominated in the majority ranges, and only relative large magnitudes exist in boundaries of the spatial-temporal domain of the model #1.

The model #2 is trained after 63,400 iterations of gradient descent, and its results are shown in Fig. 1.6. The loss and estimated α have the similar trend as that of model #1, and their values become stable in iterations of gradient descent by the L-BFGS optimizer. The final estimated α is 18.7399 $\left(\mathrm{m}^4/\mathrm{s}^2\right)$, and the relative error to the ground truth is 2.09%. The prediction of flexural guided wavefield by the model #2 is shown in Fig. 1.6c, and the difference between the predicted wavefield and the corresponding measured wavefield is shown in Fig. 1.6d. It can be seen that the prediction wavefield is close to the corresponding measured one. The results for model #1 and model #2 show that PINNs can model the pristine beam with high accuracy and consistency.

The model #3 and #4 are trained after 51,400 and 55,100 iterations of gradient descent, respectively. The difference between the predicted wavefield and the corresponding measured wavefield for the model #3 is shown in Fig. 1.7a. Large magnitudes of the difference mainly exist in the areas of damage, but others exist nearly by the areas of damage and boundaries. The difference is used to calculate $\delta(x, m)$ in a domain $(x, m) \in [5, 295] \times [1, 10]$ with a step of 0.01 for

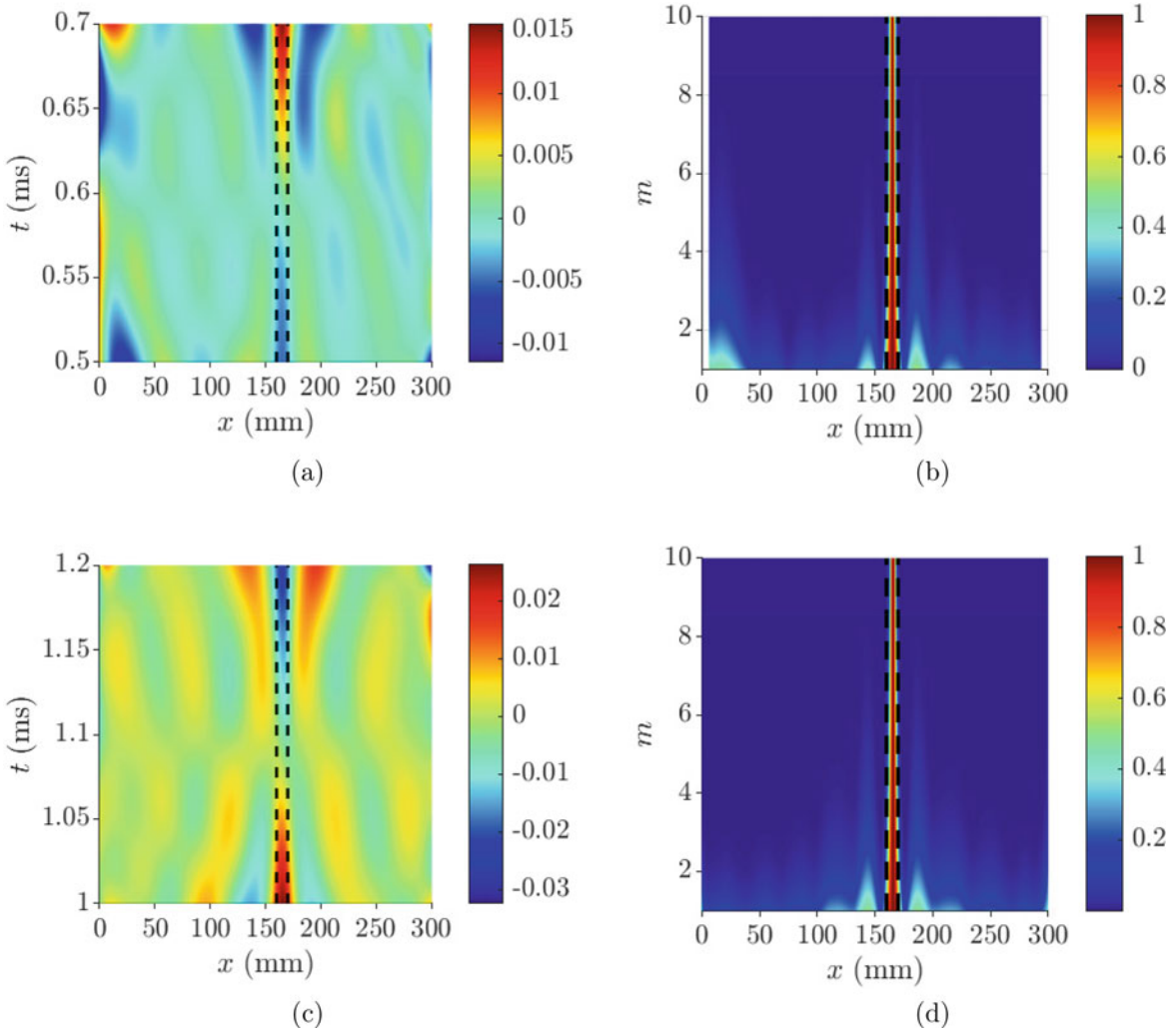

Fig. 1.7 (**a**) The difference between the predicted wavefield and the corresponding measured wavefield for model #3, (**b**) the damage identification result $\delta(x, m)$ for model #3, (**c**) the difference between the predicted wavefield and the corresponding measured wavefield for model #4, and (**d**) damage identification results $\delta(x, m)$ for model #4. Edges of the damage area are depicted by vertical dotted lines

m, which is shown in Fig. 1.7b. It can be seen that high $\delta(x, m)$ values mainly exist in the damage area so that the locations and extent of the damage can be accurately identified by the consistently high $\delta(x, m)$ values. Large magnitudes of the difference between the predicted wavefield and the corresponding measured wavefield for the model #4 also mainly exist in the areas of damage as shown in Fig. 1.7c. The difference is used to calculate $\delta(x, m)$ in a domain $(x, m) \in [0, 300] \times [1, 10]$ with a step of 0.01 for m, which is shown in Fig. 1.7d. Similarly, consistently high $\delta(x, m)$ values mainly exist in the damage area. The damage identification results for model #3 and model #4 show that the proposed method can identify the locations and extent of the damage with high accuracy and consistency.

It takes 50,700 iterations of gradient descent to train the model #5. The difference between the predicted wavefield and the corresponding measured wavefield for the model #5 is shown in Fig. 1.8a. Gaussian noise can be clearly detected in the difference, and large magnitudes of the difference exist in the damage area, boundaries, as well as nearby the damage area. The difference is used to calculate $\delta(x, m)$ in a domain $(x, m) \in [5, 295] \times [1, 10]$ with a step of 0.01 for m, which is shown in Fig. 1.8b. It can be seen that high $\delta(x, m)$ values mainly exist in the damage area, and Gaussian noise is alleviated with increasing the value of m.

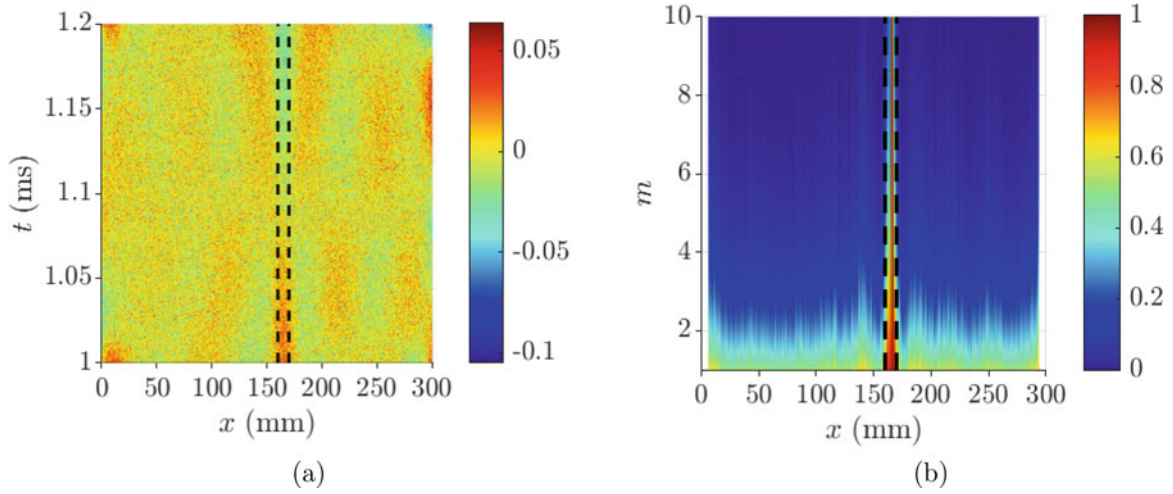

Fig. 1.8 (**a**) The difference between the predicted wavefield and the corresponding measured wavefield for model #5 and (**b**) the damage identification result $\delta(x, m)$ for model #5. Edges of the damage area are depicted by vertical dotted lines

1.4 Concluding Remarks

In this paper, a baseline-free structural damage identification method is developed for beam-like structures based on PINNs. Pseudo-pristine beam models are built by PINNs from measured flexural guided wavefields of damaged beam-like structures. A two-dimensional damage index is calculated based on the difference of the predicted flexural guided wavefields by pseudo-pristine beams and their corresponding measured flexural guided wavefields. Damage can be identified in neighborhoods with consistently high values of the damage index. The capability of modeling by PINNs is studied on the pristine beam. The results demonstrate that PINNs can accurately model the pristine beam, providing highly accurate and consistent estimates of the ratio of bending stiffness to mass per unit length. The effectiveness of the proposed damage identification method is investigated in a damage cantilever beam. It was found that (1) the proposed method can accurately identify the location and extent of damage, and (2) the proposed method is robust for measurement noise. In future works, it is worthwhile to conduct investigations on experiments by the proposed method. Besides, segmentation is only used in the temporal domain of flexural guided wavefields for better training PINNs in this study. Segmentation in the spatial-temporal domain for flexural guided wavefields can be studied when higher excitation frequencies are applied to structures.

Acknowledgments The authors are grateful for the financial support from the National Science Foundation through Grant No. CMMI-1762917.

Conflicts of Interest The authors declare no conflict of interest.

References

1. Ai, L., Soltangharaei, V., Ziehl, P.: Developing a heterogeneous ensemble learning framework to evaluate Alkali-silica reaction damage in concrete using acoustic emission signals. Mech. Syst. Signal Process. **172**, 108981 (2022)
2. Ijjeh, A.A., Ullah, S., Kudela, P.: Full wavefield processing by using FCN for delamination detection. Mech. Syst. Signal Process. **153**, 107537 (2021)
3. Abdeljaber, O., Avci, O., Kiranyaz, S., Gabbouj, M., Inman, D.J.: Real-time vibration-based structural damage detection using one-dimensional convolutional neural networks. J. Sound Vib. **388**, 154–170 (2017)
4. Yu, Y., Wang, C., Gu, X., Li, J.: A novel deep learning-based method for damage identification of smart building structures. Struct. Health Monitor. **18**(1), 143–163 (2019)
5. Ruzzene, M.: Frequency–wavenumber domain filtering for improved damage visualization. Smart Mater. Struct. **16**(6), 2116 (2007)
6. Melville, J., Alguri, K.S., Deemer, C., Harley, J.B.: Structural damage detection using deep learning of ultrasonic guided waves. In: AIP Conference Proceedings, vol. 1949, p. 230004. AIP Publishing LLC (2018)
7. Ijjeh, A.A., Kudela, P.: Deep learning based segmentation using full wavefield processing for delamination identification: A comparative study. Mech. Syst. Signal Process. **168**, 108671 (2022)
8. Song, H., Yang, Y.: Noncontact super-resolution guided wave array imaging of subwavelength defects using a multiscale deep learning approach. Struct. Health Monitor. **20**(4), 1904–1923 (2021)

9. Raissi, M., Perdikaris, P., Karniadakis, G.E.: Physics-informed neural networks: A deep learning framework for solving forward and inverse problems involving nonlinear partial differential equations. J. Comput. Phys. **378**, 686–707 (2019)
10. Cuomo, S., Di Cola, V.S., Giampaolo, F., Rozza, G., Raissi, M., Piccialli, F.: Scientific machine learning through physics-informed neural networks: where we are and what's next. Preprint (2022). arXiv:2201.05624
11. Shukla, K., Di Leoni, P.C., Blackshire, J., Sparkman, D., Karniadakis, G.E.: Physics-informed neural network for ultrasound nondestructive quantification of surface breaking cracks. J. Nondestruct. Eval. **39**(3), 1–20 (2020)
12. Rathod, V., Ramuhalli, P.: Physics-informed neural networks for identification of material properties using standing waves. In: Nondestructive Characterization and Monitoring of Advanced Materials, Aerospace, Civil Infrastructure, and Transportation XVI, vol. 12047, pp. 179–188. SPIE (2022)
13. Zhang, E., Dao, M., Karniadakis, G.E., Suresh, S.: Analyses of internal structures and defects in materials using physics-informed neural networks. Sci. Adv. **8**(7), eabk0644 (2022)
14. Hagedorn, P., DasGupta, A.: Vibrations and Waves in Continuous Mechanical Systems. Wiley (2007)
15. Doyle, J.F.: Wave Propagation in Structures: Spectral Analysis Using Fast Discrete Fourier Transforms. Springer (1997)
16. Hornik, K.: Approximation capabilities of multilayer feedforward networks. Neural Networks **4**(2), 251–257 (1991)
17. Wang, Q., Deng, X.: Damage detection with spatial wavelets. Int. J. Solids Struct. **36**(23), 3443–3468 (1999)
18. Wang, S., Wang, H., Perdikaris, P.: On the eigenvector bias of Fourier feature networks: From regression to solving multi-scale PDEs with physics-informed neural networks. Comput. Methods Appl. Mech. Eng. **384**, 113938 (2021)
19. Kingma, D.P., Ba, J.: Adam: A method for stochastic optimization. Preprint (2014). arXiv:1412.6980
20. Liu, D.C., Nocedal, J.: On the limited memory BFGS method for large scale optimization. Math. Programm. **45**(1), 503–528 (1989)